



BaTiO₃-based thermistor hollow fibers prepared using a phase inversion spinning process for energy efficient gas sorption

Jon G. Bell^{a,*}, N. Cavin^{a,b}, A.J. Knorpp^a, T. Graule^a, M. Stuer^a

^a Laboratory for High Performance Ceramics, Department of Functional Materials, EMPA, Dübendorf, Switzerland

^b Laboratory of Multifunctional Materials, Department of Materials, ETH Zurich, Zurich, Switzerland

ARTICLE INFO

Keywords:

Phase inversion
Hollow fibers
BaTiO₃
PTCR effect
Zeolites
CO₂ adsorption

ABSTRACT

Positive temperature coefficient of resistivity (PTCR) hollow fibers that exhibit self-regulating heating characteristics have potential applications in temperature-swing adsorption systems (TSA), such as CO₂ recovery and drying of compressed air. La-doped BaTiO₃ hollow fibers displaying a PTCR effect were produced by phase inverting a casting solution consisting of N-methyl-2-pyrrolidone, polymethyl methacrylate, polyvinylpyrrolidone, BaTiO₃, TiO₂, and La₂O₃ through a spinneret into a coagulating waterbath. This was followed by polymer debinding, high temperature sintering between 1350–1400 °C and annealing in air at 1175 °C to produce hollow fibers of the composition Ba_{0.9975}La_{0.0025}TiO₃. Hydrothermal synthesis was implemented to deposit an adsorbent porous zeolite X layer within the hollow fiber lumen, which was confirmed by electron dispersive X-ray spectroscopy and CO₂ adsorption at 0 °C. Hence, these materials can be applied to energy efficient TSA gas separation processes. The results are discussed in terms of hollow fiber microstructure, adsorption characteristics and electrical properties.

1. Introduction

Adsorption technologies are ubiquitously employed for the commercial production of gases [1], such as natural gas separation, air separation [2] to produce N₂ and O₂, CO₂ capture [3–5], removal of volatile organic compounds (VOCs), and moisture removal in compressed air systems [6]. Currently, gas separation technologies rely on packed beds, operating on a thermal-pressure swing adsorption-desorption cycle, which have large energy demands, long processing times (up to 8 h), and reduced separation performances [7]. This results in higher production costs and unsatisfactory purity of target species. Hollow fibers with an inner adsorbent core (such as zeolites, porous carbons or MOFs) have the potential to overcome many of the aforementioned issues associated with packed bed systems, and could be tailored for niche, compact, high-throughput applications [8]. For instance, hollow fibers assure low pressure drop and rapid heat and mass transfer [4,9], essential to achieving extremely rapid temperature swing sorption cycles; therefore, reducing the physical size of the adsorption systems and obtaining a cost-effective separation cycle. Due to the low thermal mass, hollow fiber systems can be designed to directly heat the inner adsorbent layer through Joule heating for electrothermal

desorption processes [10,11], minimizing waste heat production and requiring far less energy compared to traditional systems.

High-throughput, polymeric hollow fibers with a zeolite inner adsorbent core and an electrothermal heating layer have been previously produced using a multilayer wet spinning phase inversion process [6]. However, so far, phase inverted polymeric hollow fibers have been restricted to low temperature applications (< 100 °C) with poor recovery performance, because of the high safety risk associated with polymer degradation during electrothermal regeneration by Joule heating. This drawback can be surmounted by integrating an inorganic ceramic outer layer, which would allow for safe, high temperature, electrothermal regeneration of the adsorbent layer. The compact and simplistic nature of these systems can then be further enhanced by adding smart characteristics, such as self-regulating electrothermal desorption heating properties for adsorbent bed regeneration. Materials with self-regulating thermal properties (thermistors) exhibit a positive temperature coefficient of resistance (PTCR) effect, which can be exploited to produce smart materials that react to their environment and impart self-regulating and self-limiting temperature control [12]. Donor-doped BaTiO₃, a polycrystalline ceramic, has become one of the most widely used PTCR thermistor materials, due to its high temperature coefficient

* Corresponding author.

E-mail address: Jon.Bell@empa.ch (J.G. Bell).

<https://doi.org/10.1016/j.jeurceramsoc.2021.10.049>

Received 14 September 2021; Received in revised form 25 October 2021; Accepted 27 October 2021

Available online 29 October 2021

0955-2219/© 2021 The Authors. Published by Elsevier Ltd. This is an open access article under the CC BY license (<http://creativecommons.org/licenses/by/4.0/>).

of resistance [13–15]. BaTiO₃ is a perovskite ceramic is an electrical insulator that shows no PTCR behavior in its natural state [14]. However, after doping with aliovalent donor ions, such as La³⁺, Sb³⁺, Y³⁺, which substitute for the Ba²⁺ ion in the crystal lattice, followed by high temperature sintering and subsequent cooling in air, the material becomes conducting at room temperature and displays a large increase in resistance at the Curie point (T_C) [16–18]. At the T_C, the crystal structure changes from the ferroelectric tetragonal phase to the paraelectric cubic phase, and the PTCR effect arises due to the presence of a double Schottky energy barrier at the boundaries of semiconducting grains, which is no longer compensated by ferroelectric charges [16,19].

Phase inversion is a well-known method used for producing both porous and gas tight membranes and hollow fibers [20–22]. It is a scalable and economically viable way to shape ceramic materials, such as Al₂O₃ [23]. During phase inversion, a homogeneous polymeric solution changes from a liquid to a solid phase through a demixing process, which involves the exchange of a solvent and a non-solvent [24,25]. This method allows for a continuous and fast production process, and is typically used in the preparation of membranes for separation technologies [24]. The major advantage of phase inversion compared to extrusion is a much simpler and economic production set-up, without the initial expensive capital investment required for the extruder. However, little is known concerning the application of the phase inversion process on ceramic microstructure and functional properties post polymer debinding and ceramic sintering.

This study describes the synthesis of La-doped BaTiO₃ ceramic hollow fibers exhibiting a PTCR effect, which were prepared using a phase inversion wet spinning technique. The BaTiO₃ hollow fibers have an internal lumen diameter of approximately 1 mm and display a low pressure drop compared to traditional packed bed systems. The PTCR and self-regulating heating effect were investigated through DC resistivity vs. temperature measurements and AC voltage self-heating studies, respectively. A porous zeolite layer was deposited inside the PTCR hollow fiber lumen using a hydrothermal reaction technique. These materials have potential applications in energy efficient and self-regulating adsorbent bed regeneration for gas separation applications. The structural and electrical characteristics are discussed in terms of the synthesis route and sintering conditions. To our knowledge, this is the first instance of a BaTiO₃-based PTCR hollow fiber with an inner adsorbent zeolite layer produced by a low-cost phase inversion spinning process. Such systems could be implemented in compact and portable, high-throughput, temperature swing gas separation processes, for applications pertinent to fire and rescue, aerospace and transport.

2. Materials and methods

2.1. Materials used

Powders used in this study were Barium titanate (D_{v50} < 3 μm, 99 %, see SI for BET in Table S.3 and particle size distribution in Figure S.3) and sodium aluminate (technical grade) supplied by Sigma Aldrich and Titanium (IV) oxide (TiO₂ – rutile), 99.5 % min (metal basis) D_{v50} between 1–2 μm supplied by Alfa Aesar, CH. Lanthanum Oxide (La₂O₃) was supplied by Treibacher Industries AG with a purity of 99.998 % and D_{v50} = 1.3 μm. Zeolite 13X was acquired from Alfa Aesar, CH. Polymers used in this study were Poly(methyl methacrylate) (PMMA) with an average M.W. of 120,000 and Polyvinylpyrrolidone K90 (PVP) supplied by Sigma Aldrich. N-Methyl-2-pyrrolidone (NMP), Potassium hydroxide and sodium hydroxide were supplied by Sigma Aldrich. Silicone oil used in the oil bath for electrical testing was supplied by Fisher Scientific and had an operating range of 40 °C–200 °C. Metals for electrodes included Indium gallium alloy (In-Ga) paste (25:75 wt. %), silver paste and silver wire, 0.25 mm diameter, annealed, 99.9 % (metal basis) supplied by Fisher Scientific. N₂ (99.995 %) CO₂ (99.995 %) and He (99.995 %) gases were obtained from PanGas, Zurich used for adsorption studies.

2.2. Synthesis of Ba_{0.9975}La_{0.0025}TiO₃ hollow fibers

2.2.1. Casting solution preparation routes

2.2.1.1. Parallel addition route (BTOL-P). Following an initial slurry optimization process with undoped BaTiO₃ (details in Section 1 in SI), PMMA (5.01 wt. %), PVP (0.08 wt. %) and NMP (12.77 wt. %) were mixed in a 100 mL glass beaker. To limit NMP evaporation, the beaker was covered with Al foil and stirred at 400 RPM for 120 min at 130 °C using a combined magnetic stirrer and heating plate. After 120 min., the rotation speed was reduced to 120 rpm for 30 min. to eliminate air bubbles. Meanwhile, BaTiO₃ (68.82 wt. %), La₂O₃ (0.13 wt. %) and the small excess of TiO₂ (0.418 wt. %) was weighed and added to the ZrO₂ planetary milling container and the powders were mixed with spatula. NMP (12.77 wt. %) was weighed and added to the powders and the slurry was mixed with a spatula (therefore, PMMA + PVP + NMP + BaTiO₃+TiO₂+La₂O₃ = 100 wt. %). Following this, 3 mm milling balls were added until 50 % of the container volume was filled. The slurry was de-agglomerated for 90 min. in the planetary mill at 300 rpm. The milling balls were removed and the slurry heated to around 80 °C. When the temperature was reached, the slurry was immediately mixed with the PMMA solution. The two solutions were first mixed with a spatula and then magnetically stirred at 120 rpm and 100 °C for 10 min.. The slurry was transferred in the stainless syringe and phase inverted. The hollow fiber green bodies produced from this slurry procedure where designated the code BTOL-P, where P = parallel mixing route, i.e. mixing and de-agglomeration without PMMA and PVP polymers present (further information in section 1.2 in SI).

2.2.1.2. Series addition route (BTOL-S). PMMA (5.01 wt. %), PVP (0.08 wt. %) and NMP (25.54 wt. %) were mixed in a 250 mL glass beaker and the same mixing procedure was performed as in the BTOL-P synthesis route. Ceramic powders were prepared and weighed as stated above; however, this time the powders were added directly to the hot polymeric solution, with continuous stirring using a spatula. When the powders were well dispersed, the slurry was transferred to the planetary milling container and the aforementioned milling procedure was performed. The milling balls were removed and the slurry was transferred to the stainless syringe and phase inverted. The hollow fiber green bodies produced from this slurry procedure where designated BTOL-S, where S = series mixing route, i.e. mixing and de-agglomeration in the presence of PMMA and PVP polymers.

2.2.2. Wet phase spinning and phase inversion

Single layer hollow fibers were fabricated using a triple orifice spinneret, with external layer (d_{out}/d_{in}, 4.0/ 3.0 mm), internal layer (d_{out}/d_{in}, 2.0/1.2 mm) and bore diameter of 0.8 mm. However, only the central bore and inner bore were used for hollow fiber production. A schematic diagram of the, in-house manufactured, phase inversion spinning apparatus is shown in Fig. 1. The slurry was placed inside a 50 mL stainless steel syringe (Chemyx), and was pumped with a Harvard Apparatus PHD 2000 syringe pump into the spinneret inner bore. The internal coagulant was composed by 92.5 % wt. deionized water and 7.5 % wt. pure ethanol and was pumped to the central bore of the spinneret using a Postnova Analytics PN 1610 syringe dosing system. To avoid O-Ring abrasion, the original syringe Vitron O-ring was replaced with a Teflon O-ring (Maagtechnic, CH). The slurry and internal coagulant were delivered to the spinneret using 1/4" and 1/8" tubing, respectively, and were connected using Swagelok compression fittings. The air gap between spinneret and coagulation bath was set to 5 cm. Prior to connecting the internal coagulant tube to the spinneret, the pump was activated at 15 mL min⁻¹ with pure water for 2 min. in order to remove the air from the system. When the internal coagulant circuit was free of air bubbles then the Swagelok fitting was connected. The internal coagulant water pump was set to 12 mL min⁻¹, and during the first 20 s

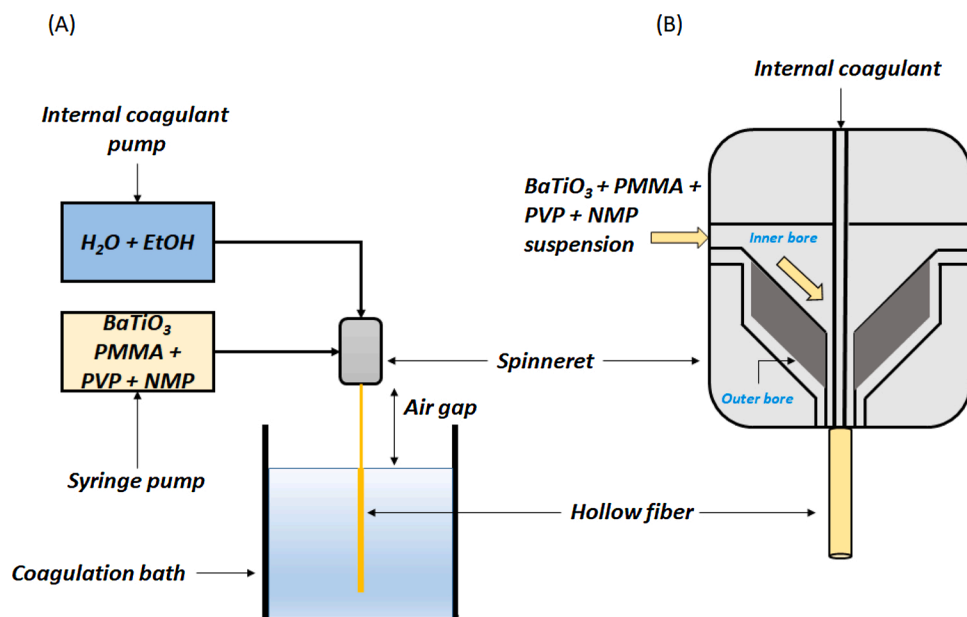


Fig. 1. Schematic representation of the hollow fiber spinning phase inversion system. (A) configuration of spinneret, internal coagulant pump, slurry syringe pump and coagulation bath. (B) Cross section of the spinneret showing the slurry pumped to the inner bore and the central bore for the internal coagulant. Only the central and inner bores were used in the study.

the water flow was not constant, as the air inside the spinneret had to be ejected. To avoid nozzle wetting, the edge of a paper towel was placed at the nozzle to adsorb the water ejected during the first 20 s. Once a stable water flow was established, the slurry syringe pump was started. The flow was set to 50 mL min⁻¹ until the slurry reached the spinneret, before the slurry flow was reduced to 5 mL min⁻¹. The fibers were collected in the water tank and then submerged in water for 12 h to remove residual NMP. Following this, the hollow fibers were dried under ambient conditions.

2.3. Debinding and sintering

PMMA burn-off was performed in a dedicated debinding furnace prior to sintering. The hollow fiber green bodies were placed on a deep-ridged Al₂O₃ ceramic plate, in order to keep the fibers as straight as possible, and inserted into the debinding furnace. The fibers were heated at a heating rate of 120 °C min⁻¹ until 300 °C. From 300 °C to 420 °C, the heating rate was reduced to 60 °C min⁻¹ and held for 120 min at 420 °C. After 120 min at 420 °C, the heating was stopped and the furnace was cooled down to room temperature. After debinding, the ceramic plate was transferred to a Nabertherm box furnace for sintering. The sintering cycle was composed of a high temperature sintering at step at 1350 °C or 1400 °C, either at 1–3 hours followed by a lower temperature air-annealing step at 1175 °C between 1–4 hours. The following sample nomenclature describes the phase inversion and sintering conditions used: BTOL-M-A-B-C, where, M is the milling procedure employed (either S or P), A is the sintering temperature (°C), B is the sintering time (hrs) and C is the annealing time at 1175 °C (hrs).

2.4. Zeolite synthesis procedure

The zeolite layer deposited within the lumen of BTOL-P-1350–2-1 hollow fibers was grown using the verified synthesis method for low silica zeolite X (FAU) with a gel molar composition of 5.5 Na₂O : 1.65 K₂O : Al₂O₃ : 2.2 SiO₂ : 122 H₂O [26]. Initially, two separate solutions were prepared. One solution was composed of sodium aluminate (Sigma Aldrich, technical grade) and deionized water, and the second solution was composed of potassium hydroxide (Sigma Aldrich, 90 wt. %), sodium hydroxide (Sigma Aldrich, 98 wt. %), and deionized water. After

an hour of mixing, the two solutions were combined. The sodium silicate (Sigma Aldrich, reagent grade) and remaining deionized water were then added to the solution and mixed for 1 h. The deionized water was added in equivalent proportions to solution 1, solution 2, and also during sodium silicate addition. A 100 mL PTFE-lined stainless steel autoclave was filled to 2/3rd total volume with the final solution, and the hollow fibers were then placed slowly in the gel to ensure that the inner hollow area was filled. The zeolite crystallization was performed under static isobaric conditions at 100 °C for 2 h. The hollow fibers were then removed and dried at 120 °C overnight. Excess zeolite on the external surface of the hollow fiber was removed by brushing with a lint free cloth. The hollow fibers were designated the code BTOL-ZEOX.

2.5. Powder X-Ray diffraction (PXRD)

The crystal structures of as-received barium titanate powder (designated code BTO), La-doped (0.25 mol. %) BaTiO₃ calcined-powder (designated code BTOL-C) and a sintered La-doped (0.25 mol. %) BaTiO₃ pellet formed from BTOL-C (designated code BTOL-PEL) were investigated through PXRD, in order to check that the La-doping procedure was successful. Due to the PXRD requirement for flat surfaced samples, a La-doped pellet was produced by milling BaTiO₃ (12.793 g), La₂O₃ (0.028) and TiO₂ (5.192 g) in 25 g of isopropanol (3 mm diameter ZrO₂ milling balls filling 50 % of the planetary milling ZrO₂ container, at 300 RPM for 90 min.) and then dried at 60 °C, before calcination at 1150 °C for 8 h (forming BTOL-C). The calcined powder (BTOL-C) was then milled in isopropanol again for 30 min. at 300 rpm. This was followed by drying at 60 °C, powder pressing and sintering at 1350 °C for 2 h, followed by annealing at 1150 °C for 1 h (see Figure S.1 in SI) to form BTOL-PEL. XRD profiles for BTO, BTOL-C and BTOL-PEL were measured on a PANalytical X'Pert Pro MPD, powered by a Philips PW3040/60 X-ray generator using Cu Kα radiation (λ = 1.540598 Å) at 40 kV and a current of 40 mA. X-Ray diffraction patterns were measured using a PW3050/60 goniometer and a PW3064/60 reflection-transmission sample stage with a revolution time of 8 s. The incident beam optics comprised a Nickel beta filter, 0.04 rad Soller slits, a 15 mm fixed incident beam mask, 1/4 ° divergence slit and a 1/2 ° anti-scatter slit. The diffracted beam optics were composed of 0.04 rad Soller slits, a 5.0 mm anti-scatter slit and a PIXcel1D-Medipix3 detector in scanning line

detector (1D) mode. The total scan time was 8.5 h and the final spectra consisted of a superposition of two runs. The program for each run employed a 5–140 2θ scanning range with a 90 ms dwell time and scan step size of 0.0033°. XRD diffraction spectra analyzed using the High Score Plus software. Following background subtraction and spectra peak determination, phases were identified and matched from the Crystallographic Open Database (COD), followed by Rietveld refinement.

2.6. Scanning Electron microscopy (SEM) and energy dispersive X-Ray spectroscopy (EDS)

Scanning electron microscopy studies were performed using a FIB/SEM System FEI Helios 660 G3 UC, FEI, in order to determine the microstructure of BTOL-P/S green bodies and their sintered analogues. Hollow fibers were directly placed on the carbon double-side adhesive tape and sputtered with a 2 nm layer of a Pd-Au using a Leica EM ACE200 vacuum coater. SEM grain size analysis was performed on the outer surface of sintered hollow fibers using Matlab's 'Linecut' program based on the line intersection method (Sven Meister (2021)). Energy dispersive x-ray spectroscopy analysis and mapping was conducted on the hydrothermally deposited zeolite layer with a Tescan SEM Vega3 fitted with Bruker XFlash 6–10 detector, and with an accelerating voltage equal to 20 kV.

2.7. Gas adsorption and density measurements

Hollow fiber surface areas were measured using N_2 gas adsorption at -196°C on a Micromeritics 2020 ASAP volumetric adsorption instrument. Degassing was performed on approximately 2 g of powder sample and approximately 1 g of green body and sintered hollow fiber material at 13 μbar and 150°C for 2 h. N_2 adsorption was performed on the degassed materials at -196°C using a high-resolution isotherm up to a N_2 relative pressure (p/p^0) equal to 0.98. Surface areas were calculated using the Brunauer-Emmett-Teller (BET) multilayer adsorption equation. Pore size distributions of green bodies BTOL-P and BTOL-S were determined from the N_2 adsorption isotherms at -196°C using the Barrett-Joyner-Halender (BJH) model. CO_2 isotherms were measured at 0°C using an ice-water slush bath. Zeolite samples were degassed for 6 h at 250°C in order to remove adsorbed moisture. Green body and sintered hollow fiber density measurements were performed using the Archimedes attachment on a Mettler XPR205 balance. Samples were dried at 60°C and pure ethanol was used for the density measurements. Measurements were performed in triplicate on approximately 0.5 g of sample.

2.8. Electrical properties

2.8.1. Hollow Fiber electrode application

Silver wire was first immersed in a 15.8 M nitric acid solution for 60 s in order to clean the surface and remove oxides, then rinsed with deionized water and dried with compressed air. Hollow fibers were broken into 2 cm long pieces and the two ends of the fiber were coated with In-Ga paste. The silver wire was rolled over the surface coated with In-Ga, and then coated with In-Ga paste. The paste was dried in a 120°C oven for 1 h. The length of the uncoated fiber (distance between the electrodes) was measured and the wall thickness was estimated from SEM images for the resistivity calculation.

2.8.2. Resistivity vs. Temperature measurements

Hollow fibres were connected to a DAQ6510 Keithley multimeter and resistance and temperature data were collected simultaneously using the Keithley Kickstart 2 software. In order to keep the fiber in position, the experimental set-up shown in Figure S.33 in SI was developed. To evaluate the resistivity behavior as a function of temperature, the set-up was placed in a programmable oven and the temperature was gradually increased with a 0.2°C s^{-1} heating rate up to 200°C .

A K-type thermocouple was placed 5 mm from the hollow fiber surface and the temperature was recorded together with the electrical resistance using a 2-wire resistance measurement. The resistivity was calculated according to the formula below

$$\rho = R \frac{A_c}{L}$$

Where ρ is the resistivity ($\Omega\cdot\text{cm}$), R is the resistance (Ω), A_c is the cross section area (cm^2) and L is the distance between the electrodes (cm). The hollow fiber wall thickness for cross section area calculation was approximated based on the SEM image of the sintered hollow fibers.

2.8.3. PTCR self-regulating heating characteristics

The self-regulating heating ability of the BaTiO_3 PTCR hollow fibers was investigated using an oil bath calorimeter system, as shown in Figure S.34 in SI. A hollow fiber bundle was made by connecting ten hollow fibers together that were wired electrically in parallel. The calorimeter was constructed by placing a glass Petri dish inside an insulating polystyrene material. The Petri dish was filled with silicon oil and the hollow fiber bundle was immersed into the oil bath. The hollow fiber bundle was suspended below the oil surface, as shown in Figure S.34 in SI. The oil bath was placed over a combined plate heater-magnetic stirrer with a magnetic stirrer inside. The oil acted as heat transfer medium for the hollow fibre module, and by changing the rotation speed, it was possible to increase or decrease the convective cooling effect of the oil on the hollow fibre bundle. The silver wire electrodes were connected to a variable transformer (voltage span 0–260 Vac and current rating 6.5 amps). The voltage was set to 234 V (90 % of the total voltage) and the power source was turned on. A current was applied to induce Joule heating and was measured with a Keithley multimeter connected in series with the hollow fiber bundle and variable transformer. The temperature of the silicon oil was measured with a TC-08 PicoLogger connected to a K-type thermocouple. To evaluate the module response to convective cooling, the measurement was started at 0 RPM and increased at 250 RPM intervals until 750 RPM was attained. The current flowing through the module was measured at all times.

3. Results and discussion

3.1. Casting solution and hollow Fiber spinning optimization

One of the goals of the hollow fiber synthesis was to attain ceramic hollow fibers with a low room temperature resistivity and PTCR effect formed through a phase inversion process. In order to obtain these characteristics, the synthesis process was developed in an iterative process. La doping methods, spinning slurry composition and spinning process parameters were optimized, as outlined in the supporting information (sections 1 and 5 in SI).

3.2. Powder X-Ray diffraction

The XRD patterns for as-received BaTiO_3 powder, BTOL-C (calcined powder) and BTOL-PEL (sintered pellet) all showed the presence of a single phase (Figure S.6 in SI). The patterns were indexed on a tetragonal unit cell and after Rietveld refinement the lattice parameters were $a = 3.9938 \text{ \AA}$ and $c = 4.0357 \text{ \AA}$ for the as-received powder. Doping with 0.25 mol. % La caused a decrease in tetragonality with $a = 3.9957 \text{ \AA}$ and $c = 4.0327 \text{ \AA}$ for BTOL-C, and $a = 3.9960 \text{ \AA}$ and $c = 4.0332 \text{ \AA}$ for BTOL-PEL (Figures S7 – S9 in SI). The variation in the lattice parameters at room temperature is consistent with a decrease in tetragonality and the values are in good agreement with those reported in the literature [27,28]. Following the observed change in tetragonality of the lattice structure, the doping and milling methods employed were successful in incorporating La into the BaTiO_3 lattice.

3.3. Scanning Electron micrographs, grain size analysis and energy dispersive X-Ray spectroscopy

3.3.1. Hollow Fiber structural characterization

Scanning electron micrographs of hollow fiber green body fracture surfaces show the presence of finger-like macrovoids and sponge-like voids, which are commonly formed during the phase inversion process [29,24]. The formation of voids is consistent with studies reported in the literature, which form due to the mutual affinity between solvent and non-solvent [30], as well mass transfer phenomenon that initiate convective flows, creating interfacial turbulence, as stated by Sternling and Scriven [31]. Recently, Guillen et al. also confirmed that macrovoid formation is due to the creation of turbulent flows of the non-solvent in the casting film [32].

The fracture surface of a BTOL-S green body, shown in Fig. 2, can be divided into several regions displaying different morphologies; with the morphological structure of the hollow fiber cross section being approximately symmetrical. A very thin and dense skin-layer is present, both on the internal and on the external surface of the hollow fiber, with a thickness of a few microns, and forms due to the rapid exchange between solvent and non-solvent, driven by a steep concentration gradient [32]. Below the skin-layer there are two regions characterized by finger-like macrovoids: one below the internal surface (internal coagulant, central bore side) and one below the external surface (external coagulant side). Between the inner and outer finger-like macrovoid region, there is a region that is free of macrovoids, characterized by an exclusively sponge-like morphology. The finger-like voids present at the external regions are generated by solvent exchange with the coagulation bath, while the finger-like voids present in the internal part, are generated by solvent exchange with the internal coagulant. At greater cross sectional depths from the external and internal surfaces, the voids increase in size, but are smaller in number.

The change in macrovoid formation with polymer loading was investigated by increasing the concentration of PMMA from 10 to 20 vol. %, which increases the viscosity from 2.5 Pa.s to 200 Pa.s (Figure S.5 in SI). Figure S.12 in SI shows the cross section of two BTOL-P green bodies with PMMA equal to 10 and 20 vol. %. The green body with the higher PMMA concentration (20 vol.%) exhibits a greater number of finger-like macrovoids (Figure S11 a, b in SI), with the voids also penetrating

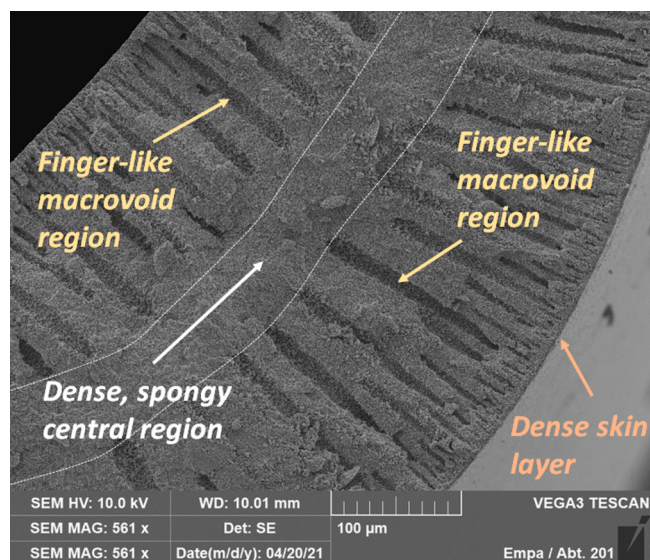


Fig. 2. Scanning electron micrograph showing the fracture surface of a BTOL-S hollow fiber green body showing void evolution and the presence of different morphological regions caused by solvent exchange (561x magnification) (For interpretation of the references to colour in this figure legend, the reader is referred to the web version of this article).

deeper below the surface compared with the green body with a PMMA concentration equal to 10 vol. % (Figure S11 c, d). Sternling and Scriven stated that the formation of macrovoids could be suppressed by increasing the viscosity of the casting solution, which reduces the percolation ability of the non-solvent. However, in this study, increasing the viscosity, by increasing the PMMA concentration, had the opposite effect. Therefore, it can be suggested that macrovoid formation appears to be a more complex phenomenon that involves the interplay between several variables, including composition, diffusivity, kinematic viscosity and surface tension [29].

The effect of sintering on the hollow fiber morphology is shown in Figure S12 in SI, which shows the fracture surface of the hollow fibers before and after sintering. During sintering, the sponge-like pores undergo closure and a clear change in the morphology can be observed, which is due to the sintering-induced densification process. However, a portion of the larger finger-like macrovoids do not completely close, leaving small voids (e.g. defects) behind. Near the fiber surface, there is an absence of finger-like voids and comparison with the corresponding green body shows that smaller voids close during sintering. This dense surface layer is believed to be essential in providing sufficient mechanical strength, analogous to honeycomb based structures; however, further investigation is required in order to optimize the micro- and macrostructure of the hollow fibers.

3.3.2. BTOL-P and BTOL-S fracture surface morphology

The influence of the milling route is depicted in Figure S13 in SI and shows that the fracture surfaces of sintered BTOL-S and BTOL-P display different morphologies. BTOL-S was dispersed in the planetary mill with BaTiO₃ already dissolved in the polymer, while BTOL-P was first dispersed in the planetary mill followed by PMMA addition after milling. These different slurry production routes result in the absence of finger-like voids in sintered hollow fibers prepared via the BTOL-S route, which may be a result of reduced particle mobility in BTOL-S, because of residual agglomerates increasing the hydrodynamic radius. These differences may cause the percolation of the non-solvent in the casting solution to change due to viscosity and mobility differences [29]. Figure S.13 also shows that the cross sections of sintered BTOL-P hollow fibers exhibit intra-granular fracture (a–d), while BTOL-S shows inter-granular fracture (e, f), supporting the hypothesis of residual porosity as a consequence of residual agglomerates in BTOL-S. This is also supported by N₂ adsorption (Table S.3 in SI) density (Table 1) and electrical measurements, which show an increased porosity, lower density, higher low temperature resistivity and increased PTCR magnitude (Fig. 7c) for the BTOL-S-1350–2-1 specimen compared to all other sintered specimens studied.

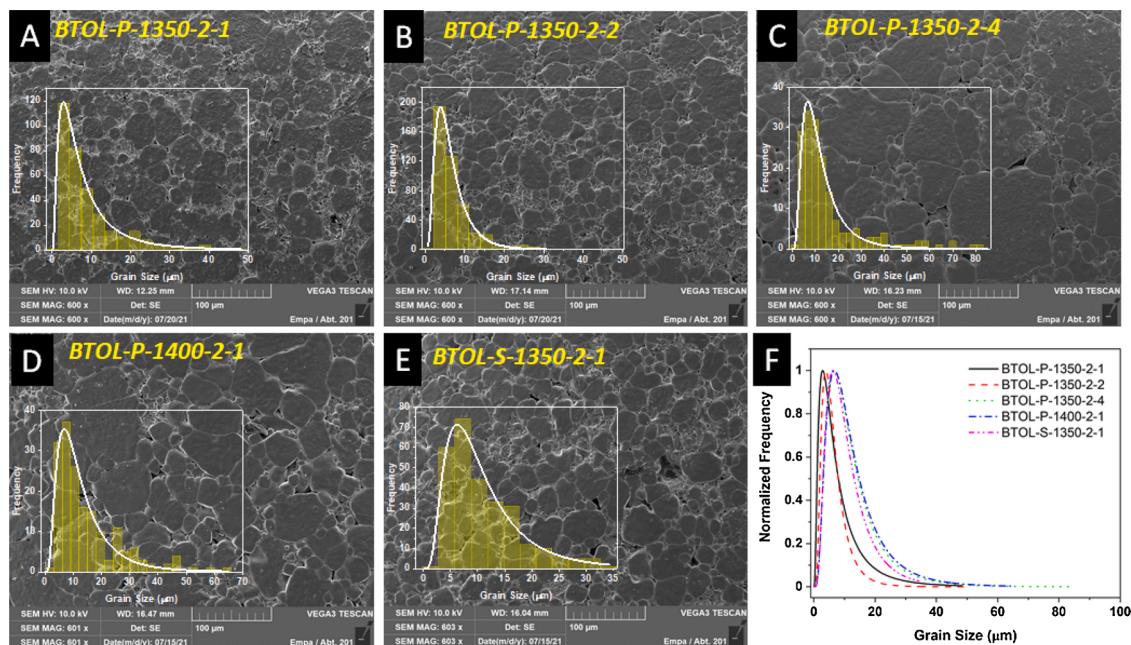
3.3.3. Effect of sintering schedule on grain size

SEM images of the outer surfaces of sintered hollow fibers, as a function of sintering and annealing conditions, are shown in Fig. 3 a–e. The grain size distributions were calculated using the line intersection method with a 3D grain diameter to 2D lineal intercept ratio equal to 1.6, assuming a lognormally distributed grain size, as reported by Gerlt et al. and Mendelson [33,34]. Histograms calculated from the line intersection method and the corresponding lognormal distribution fittings are shown in Fig. 3 insets. The lognormal fitting parameters are shown in detail in Figures S.14 – S.21 in SI. The intersection analysis was only performed on one SEM image per fiber, which is sufficient for a qualitative but not a quantitative assessment. The parameters μ (μ) and σ (σ), derived from lognormal distribution fitting, define the mean and the distribution width, respectively, and are reported in Table 1 for the BTOL-P sintered series and BTOL-S-1350-2-1 specimens. BTOL-P samples sintered at 1350 °C and annealed for longer times at 1175 °C show an increase in the mean and maximum grain size, as the mean grain diameter increases from 8.9 μ m for BTOL-1350-2-1 to 12.7 μ m for BTOL-1350-2-4. The maximum grain size also increases significantly from 47 μ m to 82 μ m for the aforementioned specimens,

Table 1

Grain distribution characteristics from lognormal fitting of green bodies and sintered specimens studied and their corresponding densities.

Specimen		Sintering Conditions			Grain Size				Density
Route	Type	A	B	C	μ (μm)	σ	Min (μm)	Max (μm)	Arch. (g/cm^3)
BTOL-P	HF	1350	2	1	8.9 ± 0.4	9.5 ± 1.0	0.2	47.3	5.34 ± 0.19
	HF	1350	2	2	6.7 ± 0.1	4.4 ± 0.2	0.8	44.4	5.14 ± 0.12
	HF	1350	2	4	12.7 ± 0.5	9.3 ± 0.8	1.2	81.7	4.92 ± 0.06
	HF	1400	2	1	13.2 ± 0.9	10.0 ± 1.4	1.8	63.5	5.05 ± 0.12
BTOL-S	HF	1350	2	1	11.4 ± 0.7	8.0 ± 1.1	1.4	31.8	4.71 ± 0.11

Type HF = sintered hollow fiber, A = Sintering temperature ($^{\circ}\text{C}$), B = sintering time (hrs), C = annealing time (hrs).**Fig. 3.** Scanning electron micrographs and grain size distribution with lognormal fitting (inset) for (a) BTOL-P-1350-2-1, (b) BTOL-P-1350-2-2, (c) BTOL-P-1350-2-4, (d) BTOL-P-1400-2-1, (e) BTOL-S-1350-2-1, and (f) comparison of the normalized lognormal fits to the histogram data.

respectively. Sintering at 1400°C also increases the mean grain diameter to $13.2\ \mu\text{m}$ and slightly increases the width of the lognormal distribution. Similar trends are observed for BTOL-P-1400–2-3 (shown in Figure S.14 in SI), with $\mu = 19\ \mu\text{m}$ and $\sigma = 16.2$, indicative of continued grain growth and broadening of the grain size distribution width with longer annealing times. BTOL-S-1350–2-1 has a slightly larger mean grain size of $13\ \mu\text{m}$, but a smaller maximum grain size of $32\ \mu\text{m}$ and narrower distribution width of 8.0 compared to the BTOL-P-1350–2-1 analogue. However, due to the lower density of BTOL-S (Table 1) and showing higher porosity (Fig. 3a vs. e), this may support the theory that residual agglomerates remain during the BTOL-S production route. From the BTOL-P series, it appears that sintering at higher temperature or annealing for longer times increases the mean and maximum grain diameter, and increases the distribution width, as shown in Fig. 3f. In this study, grain growth and grain boundary oxidation occur simultaneously during the annealing stage, which according to LaCourse et al. should increase the grain boundary Schottky barrier due to chemisorption of oxygen [35]. Hence, these competing processes will determine the electrical properties. Grain growth will reduce the grain boundary volume fraction and decrease the PTCR magnitude, while the presence of larger grains results in a lower room temperature resistivity. Conversely, oxidation for longer times at 1175°C will increase the PTCR magnitude and room temperature resistivity. Additionally, the formation of pores during sintering and annealing will increase the room temperature resistivity, but can also increase the PTCR magnitude, as reported by Zhang et al. [36].

Archimedes density measurements for the BTOL-P sintered series

and BTOL-S-1350-2-1 are reported in Table 1. The density of a pressed pellet, coded BTOL-PEL, was $5.69 \pm 0.03\ \text{g cm}^{-3}$, equivalent to 94 % of the theoretical density of BaTiO_3 . Sintered hollow fibers derived from phase inverted green bodies show densities ranging from $5.34 \pm 0.19\ \text{g cm}^{-3}$ for BTOL-1350-2-1 to $4.71 \pm 0.11\ \text{g cm}^{-3}$ for BTOL-S-1350-2-1, which corresponds to 88.6 % and 78 % of the theoretical density, respectively. Additionally, increasing the annealing time and sintering temperature of the BTOL-P series hollow fibers decreased the density, while BTOL-S-1350-2-1 shows the lowest density of the series studied. This demonstrates that phase inverted green bodies can be sintered to relatively high density. Some open porosity may be generated as grain growth occurs, as reported in section 7 in SI, and this reduces the sintered densities. Simultaneous grain growth and pore growth has been attributed to an evaporation-condensation mechanism [37], with particle size distribution, presence of aggregates and impurities, and sintering atmosphere being important factors affecting the rate and degree of pore formation. The presence of aggregates in BaTiO_3 green bodies could result in the formation of pores during sintering, as has been observed in the formation of dense alumina tubes [37]. It is clear that further optimization of the powder dispersion and sintering strategies are required in order to obtain densities that strike a balance between mechanical strength and PTCR effect characteristics.

3.3.4. Zeolite deposition characterization

Simultaneous co-spinning of a multilayer PTCR outer layer and a zeolite inner layer was not possible, as the zeolite layer would suffer high temperatures during the BaTiO_3 sintering and annealing process. It

has been shown for ZSM-5 zeolites that heating above 1000 °C caused a significant reduction in the surface area, with areas decreasing from 300 to $< 10 \text{ m}^2 \text{ g}^{-1}$ after heating to 1150 °C [38]. Consequently, such a large reduction in porosity would dramatically decrease the zeolite's adsorption capacity and ability to adsorb species such as CO_2 and H_2O in adsorption-based separations. Therefore, the adsorbing zeolite layer must be deposited after the ceramic fiber has been sintered. Several studies have reported the use of hydrothermal synthesis for depositing zeolitic layers within ceramic hollow fibers, which was the technique employed in this study [39,40]. Fig. 4 shows a SEM cross section of BTOL-1350-2-1 hollow fiber after the hydrothermal synthesis of zeolite X (forming BTOL-ZEOX). It is evident that a zeolitic layer had formed within the hollow fiber lumen, with zeolite X particles exhibiting a diameter of approximately 2 μm , which is also visible in Fig. 5 (top left SEM image). The total amount of zeolite deposited within the lumen was 0.09 g on 0.52 g of hollow fiber, which is equal to a deposition ratio of 21 wt. %. The zeolite deposition method requires further optimization and the amount deposited can be increased by performing a multi-stage synthesis, which repeats the deposition process multiple times on the same sample [39].

Fig. 5 shows electron dispersive x-ray spectroscopy (EDS) elemental spatial mapping with Al and Si originating from the deposited zeolite particle cluster, against a background of Ba, Ti and La originating from the hollow fiber lumen surface layer. EDS analysis confirmed the expected chemical composition for zeolite X with a 1:1 Si: Al ratio with K and Na present as counter ions (Figure S.22 in SI). Additionally, EDS spatial mapping also indicated that BaTiO_3 was successfully doped with La.

4. Gas adsorption measurements

4.1. N_2 adsorption

Nitrogen adsorption isotherms at -196°C on BTOL-P and BTOL-S green bodies are shown in Figure S.24 in SI and are classified as Type 2 in the IUPAC classification scheme. Surface areas derived from BET analysis of N_2 isotherms (Figure S.25 and Table S.3 in SI) show that BTOL-P has a slightly higher surface area of $7.13 \pm 0.61 \text{ m}^2 \text{ g}^{-1}$ compared to $5.03 \pm 0.76 \text{ m}^2 \text{ g}^{-1}$ for BTOL-S. BJH analysis of N_2 isotherms (see Figure S.26 in SI) show that the pore size distributions of BTOL-P and BTOL-S green bodies are approximately similar, with the incremental pore area ($\text{m}^2 \text{ g}^{-1}$) increasing dramatically over the

macropore range 10–100 nm. Table S.3 shows N_2 BET surface areas of BTOL-P series sintered hollow fibers and BTOL-S-1350-2-1, derived from BET model fitting (Figure S.27 in SI). The surface areas of all specimens studied were reduced below $0.2 \text{ m}^2 \text{ g}^{-1}$ after sintering; therefore, the measurements are only pseudo quantitative in nature. This is due to the large uncertainty associated with N_2 adsorption for such low surface areas, and where krypton adsorption is commonly employed for a more accurate measurement, due to its lower vapour pressure at -196°C [41]. BTOL-P series specimens either annealed for 4 h or sintered at 1400 °C, and BTOL-S-1350-2-1 prepared via the series milling route, exhibit higher surface areas compared to BTOL-P-1350 specimens annealed for 1 and 2 h. This increase in surface area is coincident with a decrease in specimen density, validating the theory that pores are developed in these materials during grain growth, and full densification is not attained. N_2 adsorption for BTOL-ZEOX containing a zeolitic lumen layer could not be measured due to activated diffusion effects at -196°C . This is indicative of the predominance of constricted ultra-microporosity ($< 0.7 \text{ nm}$).

4.2. CO_2 adsorption and characterization of zeolitic layer

The porous structure of microporous materials is routinely characterized using CO_2 adsorption at 0°C [42,43]. Adsorption at this temperature ensures that activated diffusion effects, associated with N_2 adsorption at -196°C , are negated and accurate pore volumes can be determined. The subcritical CO_2 adsorption isotherms for the deposited zeolite X layer (assuming CO_2 is solely adsorbed on 0.09 g of zeolite) and a BTOL-P-1350-2-1 hollow fiber are shown in Fig. 6. The hollow fiber adsorbed a negligible amount of CO_2 and was not porous. The isotherm for the deposited zeolite layer (BTOL-ZEOX) is described as Type 1 in the IUPAC classification scheme, which indicates a predominantly microporous material. Approximately $12 \text{ cm}^3 \text{ g}^{-1}$ of CO_2 (STP) are adsorbed at 1 bar, with a steep uptake region at low pressure with $7.1 \text{ cm}^3 \text{ g}^{-1}$ (STP) adsorbed at 50 mbar. These values can be contrasted with $138 \text{ cm}^3 \text{ g}^{-1}$ CO_2 (STP) at 1 bar and $85 \text{ cm}^3 \text{ g}^{-1}$ (STP) at 50 mbar for zeolite 13X (Figure S.28 in SI). Therefore, the amount of CO_2 adsorbed for the deposited zeolite layer is approximately an order or magnitude lower over the entire pressure range studied, compared to the commercial zeolite, which is commonly used in gas separation applications.

The volume of microporous materials with a pore diameter $< 0.7 \text{ nm}$ can be calculated using the Dubinin-Radushkevich (D-R) equation [44], which is defined as follows:

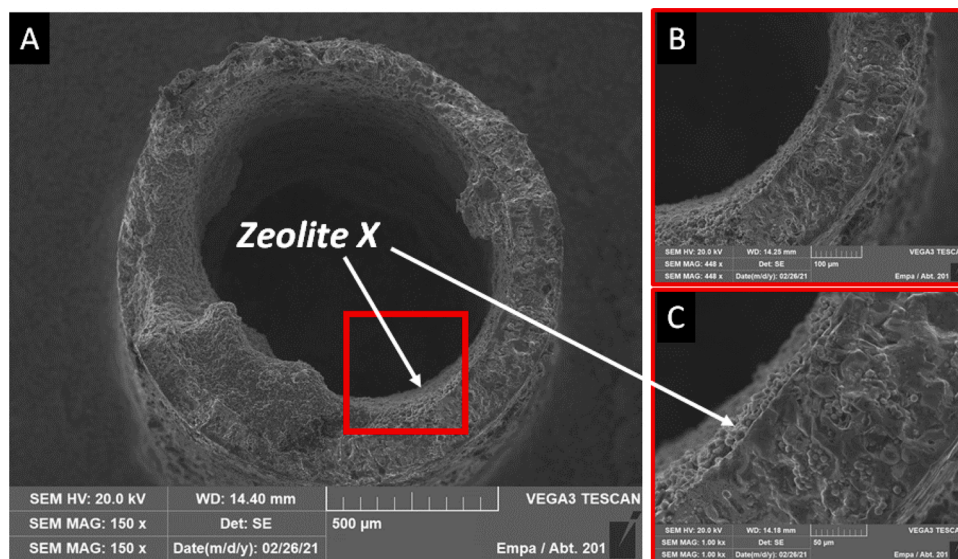


Fig. 4. Scanning electron micrograph showing the deposition of zeolite X using a hydrothermal method. (A) Fracture surface of BTOL-ZEOX at 150x magnification, (B) 448x magnification and (C) 1000x magnification.

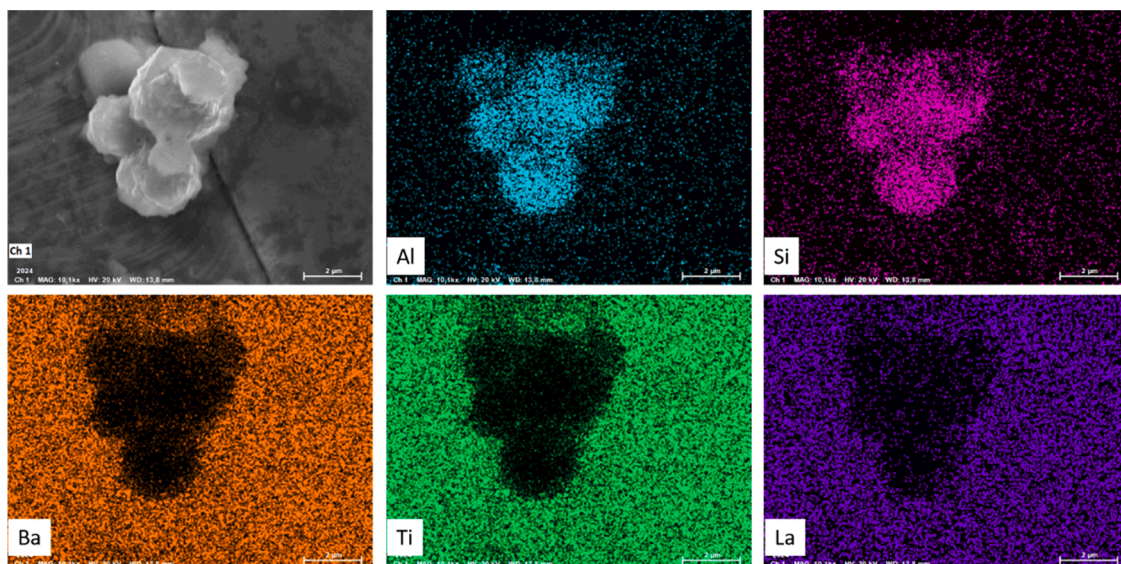


Fig. 5. Electron dispersive x-ray spectroscopy (EDS) spatial mapping images showing isolated zeolite particles within the hollow fiber lumen of BTOL-ZEOX. The zeolite layer and the hollow fiber can be clearly distinguished. The zeolite is composed of silicon and aluminum with a stoichiometric ratio of 1:1, which is distinguished from the hollow fiber lumen surface containing Ba, Ti, and La.

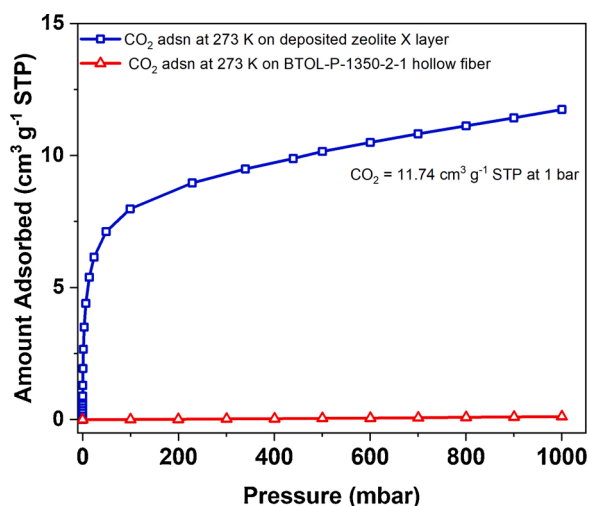


Fig. 6. CO₂ adsorption isotherms at 0 °C for (a) the zeolite inner layer deposited by hydrothermal synthesis (BTOL-ZEOX) and (b) the sintered hollow fiber BTOL-P-1350-2-1 without a zeolitic inner layer.

$$\log_{10} = \log_{n_0} - D \log^2 \left(\frac{p^\circ}{p} \right)$$

Where n is the amount adsorbed (mmol g^{-1}), n_0 is the amount adsorbed corresponding to the micropore volume (mmol g^{-1}), p is the pressure (mbar) and p° is the saturated vapour pressure (mbar), and D is a constant that is related to the microporous structure of the adsorbent. The ultramicropore ($< 0.7 \text{ nm}$) volume of the deposited zeolite X layer was determined by carbon dioxide adsorption at 0 °C ($p\text{CO}_2 = 1.032 \text{ g cm}^{-3}$) followed by interpretation by the D–R model, and the results are given in Table S.4. The linear low pressure region of the D–R graphs were extrapolated to $p/p^\circ = 1$ to obtain the amount corresponding to the micropore volumes ($\text{cm}^3 \text{ g}^{-1}$) and showed high linearity, as shown in Figures S.29–30 in SI. BTOL-ZEOX has a micropore volume equal to $0.026 \text{ cm}^3 \text{ g}^{-1}$ compared to $0.32 \text{ cm}^3 \text{ g}^{-1}$ for the commercial 13X zeolite, which is again an order of magnitude lower. This implies that the ultramicropore size distribution is very narrow with a limited adsorption

capacity.

The Henry's law parameter (K_H) describes the strength of interaction between the adsorbate and the surface. The Henry's law constants can be obtained by a virial equation analysis of the isotherm data. The virial equation can be written as follows [45]:

$$\ln \left(\frac{n}{p} \right) = A_0 + A_1 n + A_2 n^2 \dots$$

Where n is the amount adsorbed (mol g^{-1}) at pressure p (Pa). The first virial coefficient A_0 ($\text{mol g}^{-1} \text{ Pa}^{-1}$) is related to the Henry's law constant K_H and at low surface coverage the virial equation reduces to Henry's Law [46]. Therefore, $K_H = \exp(A_0)$, where K_H is dependent on the interaction between the adsorbed molecule and the adsorbent surface. The higher polynomial terms A_2 etc. can be neglected at low surface coverage and a linear graph of $\ln(n/p)$ vs. n is obtained. A_0 is the linear equation intercept and quantifies the adsorbent-adsorbate interactions, while the gradient A_1 describes the adsorbate-adsorbate interactions. The equation has been derived from both thermodynamic [47] and kinetic [48] perspectives for adsorption at low surface coverage. A_0 , A_1 and K_H values for CO₂ at 0 °C adsorption were obtained from linear fitting of graphs of $\ln(n/p)$ vs. p for BTOL-ZEOX and 13X and are shown in Figures S.31–32 in SI, respectively, and the values given in Table S.4. The Henry's law constants (K_H) derived from virial A_0 values are $0.35 \pm 0.02 \times 10^{-5} \text{ mol g}^{-1} \text{ Pa}^{-1}$ for BTOL-ZEOX, which is approximately 1/4 lower compared to $1.19 \pm 0.03 \times 10^{-5} \text{ mol g}^{-1} \text{ Pa}^{-1}$ for 13X zeolite. In contrast, carbon molecular sieves have A_0 values equal to $-16.344 \pm 0.005 \ln(\text{mol g}^{-1} \text{ Pa}^{-1})$ at 30 °C, which corresponds to a Henry's law constant equal to $8 \times 10^{-8} \text{ mol g}^{-1} \text{ Pa}^{-1}$ [49]. The much higher K_H values of zeolites are indicative of strong electrostatic forces between the quadrupolar CO₂ molecule and the zeolite surface at low pressure. The high A_1 value of BTOL-ZEOX ($A_1 = -12951 \text{ mol g}^{-1}$) is indicative of the presence of confined porosity, which increases adsorbate-adsorbate interactions.

Molecular dimensions of molecules are an important factor when understanding molecular exclusion as well as shape and size selectivity in porous materials [49]. Molecular cross sections derived from ZINDO molecular orbital calculations have shown that one critical dimension is required for access to slit shaped pores, while two minimum dimensions are required for access to cylindrical pores, which for CO₂ have values of MIN-1 = 3.189 \AA and MIN-2 = 3.339 \AA [50]. Hence, the pores formed in

BTOL-ZEOX have pore diameters greater than these dimensions assuming cylindrical pores are formed, and tailoring of the zeolite synthesis procedure may be possible to increase selective adsorption for molecular sieving applications [51]. However, it is evident that further optimization of the zeolite growth method is required in order to increase the micropore volume for low partial pressure adsorption, where accessible pore volumes are essential for adsorption- and catalytic-based applications.

5. Electrical characterisation

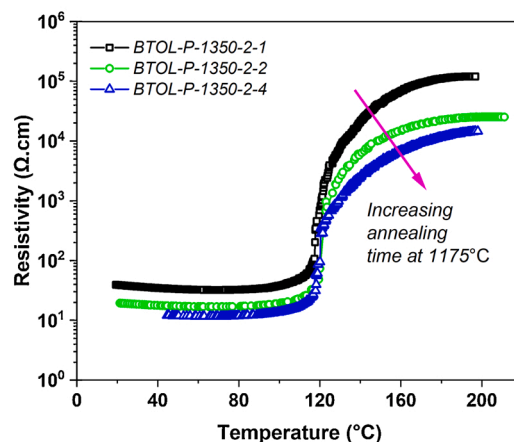
Samples prepared by the direct doping route all displayed the characteristic color change from off-white, for undoped BaTiO_3 , to a blue/grey color, indicative that the material had transitioned from an insulating p-type material to an n-type semiconducting material with a low room temperature resistivity [52]. Compositions mixed for insufficient time in the planetary mill did not display a blue-grey color and were not electrically conductive after sintering. The planetary milling time is a crucial step for successful La incorporation. Only compositions milled for 90 min. allowed for a fine homogeneous distribution of the oxide precursors, required for efficient solid reaction and thus electrical conductivity, post sintering.

5.1. Resistivity vs. Temperature profiles

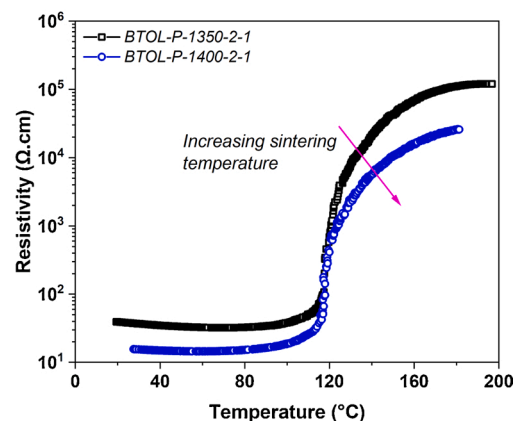
Fig. 7a shows the resistivity vs. temperature response for BTOL-P series hollow fibers sintered at 1350 °C and annealed at 1175 °C for 1, 2 and 4 h. The electrical parameters are reported in Table 2. It is evident that all hollow fibers studied show a marked PTCR effect, with the resistivity increasing by several orders of magnitude at the Curie temperature of BaTiO_3 . Increasing the annealing time from 1 to 4 h decreases the low temperature resistivity (ρ_{50}) from 33 to 12 $\Omega\cdot\text{cm}$, respectively, and decreases the maximum resistivity from 3.3 k $\Omega\cdot\text{cm}$ to 1 k $\Omega\cdot\text{cm}$ and 100 k $\Omega\cdot\text{cm}$ to 11.5 k $\Omega\cdot\text{cm}$, respectively. These trends correspond to an increase in grain size, which will decrease the volume fraction of highly resistive grain boundaries. Increasing the sintering temperature to 1400 °C had a similar effect, as shown for BTOL-P-1400-2-1, due to continued grain growth during sintering and annealing, as shown in Fig. 7b. LaCourse reported that increasing the annealing time at 1175 °C increased the PTCR intensity and room temperature resistivity [35]. This was explained due to enhanced oxygen chemisorption at the grain boundaries, resulting in larger Schottky barriers. However, a lower volume fraction of grain boundaries would result if grain growth continues and this would decrease PTCR intensity and the room temperature resistivity. Therefore, the observations in this study are contrary to those of LaCourse, and this is due to competing grain growth and grain boundary oxidation during the annealing phase at 1175 °C [35]. In LaCourse's study, only grain boundary oxidation occurred during the annealing phase. Additionally, pore formation during sintering and annealing could play a role, as the surface area increases and density decreases with increasing annealing time, or higher sintering temperatures. This additional competing mechanism would result in higher room/ low temperature resistivities, but higher PTCR magnitudes, due to increased oxidation kinetics of the grain boundaries facilitated by transport porosity [36].

The influence of the milling route on the electrical properties is shown in Fig. 7c. BTOL-S-1350-2-1 has a much higher resistivity at 50 °C (ρ_{50}) of 72 $\Omega\cdot\text{cm}$ compared to the BTOL-P series and the largest resistivity maximum ($\rho_{\text{Max}} = 141 \text{ k}\Omega\cdot\text{cm}$) out of all samples studied (see Table 2). Moreover, the PTCR intensity is theoretically the largest; however, the range of the multimeter was exceeded at 136 °C, limiting direct comparison between samples at higher temperatures. Fracture surfaces shown in Figure S.13 in SI demonstrate BTOL-S-1350-2-1 underwent inter-granular fracture, and this could be due to the presence of porosity, as confirmed by density and N_2 adsorption measurements (Table 1 and Table S.3 in SI, respectively). There are clear differences in

a)



b)



c)

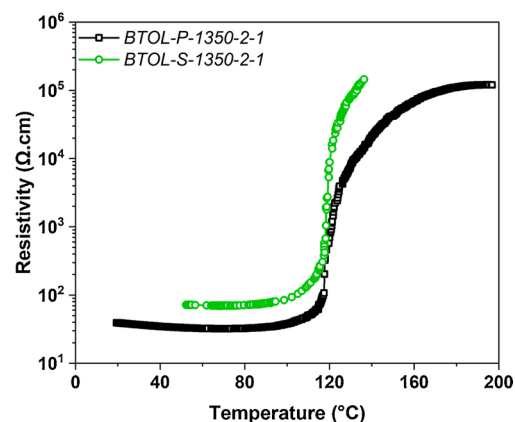


Fig. 7. Resistivity (ρ in $\Omega\cdot\text{cm}$) vs. temperature ($^{\circ}\text{C}$) for BTOL-P series hollow fibers showing (a) the effect of annealing time at 1175 °C and (b) sintering temperature on the PTCR characteristics. The effect of the parallel or series deagglomeration mixing route is shown in (c) for hollow fibers sintered at 1350 °C for 2 h and annealed at 1175 °C for 1 h.

Table 2

PTCR parameters for 0.25 mol. % La-doped BaTiO₃ hollow fibers specimens studied, determined from resistivity vs. temperature oven profiling.

Sample	Resistivity at 50 °C (Ω.cm)	Log(ρ_{\max}) at (180 °C) (Ω.cm)	PTCR Intensity Log (ρ_{\min}/ρ_{\max})
BTOL-P-1350–2-1	33.40	5.04	3.52
BTOL-P-1350–2-2	17.30	4.35	3.11
BTOL-P-1350–2-4	11.90	4.06	2.98
BTOL-P-1400–2-1	14.50	4.40	3.24
BTOL-S-1350–2-1	72.10	5.16*	3.30*

* The resistivity reading for BTOL-S-1350–2-1 exceeded the range of the multimeter at 136 °C. In this study, the low temperature resistivity was compared at 50 °C, due to missing data due to a logging error.

the electrical properties depending on whether de-agglomeration occurred in the absence (BTOL-P) or presence of PMMA (BTOL-S).

For BTOL-S, de-agglomeration in the polymeric solution may promote physisorption of PMMA on the BaTiO₃ particles, which could result in smaller agglomerate sizes. Increased dispersion has been observed for BaTiO₃ nanoparticles due to the adsorption of ammonium acrylate-methyl acrylate (PAA50), resulting from interaction between COO[−] polymer groups and surface Ba²⁺. Therefore, a similar mechanism may also occur between Ba²⁺ and the ester groups of PMMA [53]. However, BTOL-S-1350-2-1 has the lowest density and highest surface area of all specimens studied, which suggests that PMMA inhibits de-agglomeration, which promotes pore formation during sintering. The presence of pores will increase the low temperature resistivity and increase the PTCR magnitude [36], which is observed for BTOL-S-1350-2-1. Conversely, BTOL-P sintered specimens, which were not de-agglomerated in PMMA polymer, had higher densities and lower surface areas suggesting improved de-agglomeration in the absence of PMMA. Consequently, lower room temperature resistivities and a smaller PTCR magnitude should be theoretically observed, which was confirmed experimentally in this study. The results indicate that the milling and de-agglomeration route strongly influence the PTCR characteristics; however, additional work is required to understand these processes.

The resistivity of BaTiO₃-based PTCR materials above the Curie temperature can be described by the Heywang model [16,14], which is based on the formation of a potential barrier at the grain boundaries and is defined in the equation below.

$$\rho = A \exp\left(\frac{e\phi_0}{kT}\right)$$

Where A is a constant, e is the elementary charge and ϕ_0 is the barrier height in eV. The barrier heights for BTOL-P and BTOL-S sintered series were calculated from graphs of $\ln(\rho)$ vs. $1/T$ graphs (Figure S.35 in SI). The plots reveal the presence of three linear regions in the temperature ranges: (region 1) 128–143 °C, (region 2) 143–162 °C and (region 3) 162–181 °C for all specimens studied (Table S5 in SI). The non-linearity of the graphs for $T > T_C$ suggests that the barrier term may be temperature dependent. In regions 2 and 3, above the Curie temperature, the barrier heights are in the range 0.38 – 0.72 eV. These values are lower compared to those reported by Kuwabara [54], which range from 0.65 – 0.9 eV for donor-doped BaTiO₃ PTCR materials with densities in the range 71–78 % of the theoretical BaTiO₃ density. Kuwabara also reported a PTCR intensity of 6–7 orders of magnitude, whereas this study reports only a 3–4 order of magnitude increase. Consequently, these differences may be attributed to Kuwabara's lower sample densities, which could result in a higher degree of oxidation, increasing the barrier height. The relationship between barrier heights and microstructural

parameters is complex, and there are no clear trends between grain size and density. The number of articles reporting the detailed interrelationship between microstructure, chemistry and electrical properties are very few and this should be a future area of study.

5.2. Self-regulating heating characteristics

Figs. 8 and 9 show the power and oil temperature vs. time profiles of a fiber bundle composed of ten BTOL-01-1350-2-1 fibers, which were immersed in an oil bath. On application of 234 V, the initial power response (0–50 s, in Fig. 8) increases rapidly to 55 W. As the surface temperature of the hollow fiber increases, due to the Joule heating effect, then the resistance of the bundle increases in parallel. At $T = 120$ °C, the resistance reaches the exponential phase of the resistance vs. temperature profiles and the power decreases and reaches a steady state value of 15 W. The time taken to go from a peak power of 55 W to the steady state power of 15 W is approximately 7 s. This rapid heating of the material is due to the low thermal mass of the hollow fibers. The rate of power decrease and the steady state values are a function of the convective cooling rate of the surrounding oil medium, which determines the hollow fiber surface temperature. The power consumption decreases gradually as the oil continued to heats, due to a decrease in the heat transfer rate and a corresponding increase in the hollow fiber bundle resistance (Figure S.36 in SI).

Fig. 9 shows the effect of changing the rate of convective cooling on the hollow fiber bundle power consumption by changing the mixing speed of the oil bath calorimeter. Switching the stirring from 0 to 250 rpm results in a power increase up to 20 W with a corresponding decrease in the temperature of the silicon oil bath. The sudden decrease in temperature is due to the presence of a thermal gradient, which exists prior to stirring and is eliminated once convective mixing is initiated. As the temperature of the oil, surrounding the hollow fiber bundle, decreases then heat transfer increases and the hollow fiber surface temperature is lowered. This results in an increase in power that raises the hollow fiber surface temperature. Therefore, heat flows to the oil bath and a new thermal equilibrium is achieved, causing an increase in resistance of the bundle. Hence, a self-regulating thermal feedback process is in operation and is dependent on the temperature of the surrounding environment, which is controlled by the rate of convective cooling. When the rotation is increased incrementally from 250 to 750 rpm then the power rapidly reaches a new equilibrium value for each stirrer speed. Increasing the mixing speed results in a transient increase in power consumption for the module. When thermal equilibrium is

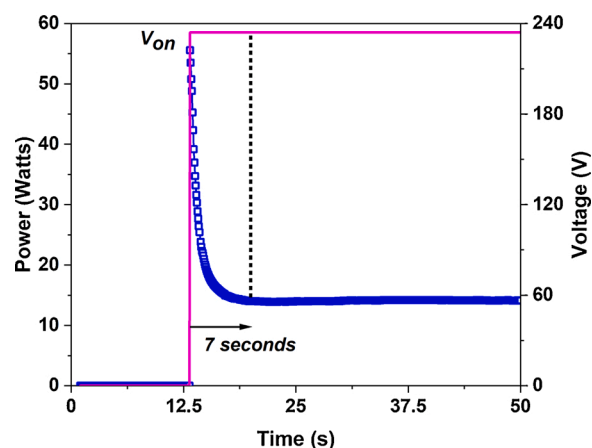


Fig. 8. Graph of power (W) vs. time (s) for the BTOL-P-1350-2-1 hollow fiber bundle in a static oil bath (magnetic stirrer speed = 0 rpm). At 12.5 s, there is an initial power spike as the voltage is switched from 0 V to 234 V. For times > 7 s, the power decreases to 15 W and gradually decreases as the temperature of the oil bath increases.

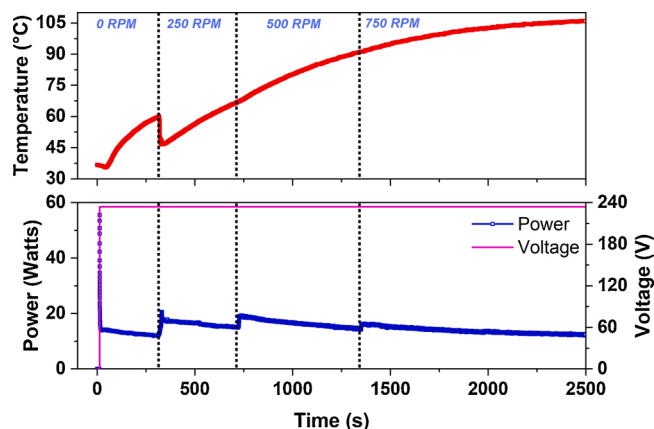


Fig. 9. Graph showing calorimeter oil bath temperature ($^{\circ}\text{C}$) and power (Watts) vs. time (s) for a BTOL-P-1350-2-1 hollow fiber bundle immersed in a silicon oil, for magnetic stirring speeds: 0, 250, 500 and 750 RPM. The change in power consumption with increasing convective cooling rates (increasing stirring speed) demonstrates that the self-regulating heating of BTOL-01-1350-2-1 is in operation.

reached between the oil and hollow fiber surface then the power decreases gradually. These observations are consistent with typical thermistor behavior, which is due to the PTCR effect [12].

Previous work on polymeric PTCR hollow fibers has shown that the optimum self-regulating and self-limiting heating behaviour requires a sharp PTCR transition to the high resistance state at the Curie temperature, which was also achieved in this study [6]. This ensures that the device is protected from over-voltage and over-current scenarios during zeolite regeneration. Furthermore, the power consumption of the system will respond rapidly to changes in gas flow rate, as the material will be highly sensitive to changes in the convective cooling rate at temperatures close to the Curie temperature, resulting in effective self-regulating heating during adsorbent bed regeneration. Additionally, temperatures $> 100^{\circ}\text{C}$ are required for the desorption of target species such as H_2O from zeolite X materials. Thermogravimetric studies on H_2O desorption from zeolite 13X have shown that at 100°C approximately 70–80 % of the adsorption capacity is recovered, which is more than sufficient for effective H_2O adsorption in TSA applications [6]. In contrast, CO_2 can be desorbed at lower temperatures of around 50°C , as shown by Larasati et al. [55]. Therefore, the PTCR characteristics of BaTiO_3 hollow fibers presented in this study are suitable for effective regeneration of the adsorbent zeolite bed, as the system will drive to temperatures $> 100^{\circ}\text{C}$ but $< 120^{\circ}\text{C}$. Therefore, these materials could be utilised in applications for H_2O removal from compressed air lines, as well as CO_2 separation and purification.

6. Conclusions

This study has successfully produced PTCR La-doped BaTiO_3 hollow fibers for gas separation applications through a combination of direct donor-doping, low-cost phase inversion and post-sintering hydrothermal zeolite synthesis. PMMA was found to be an excellent candidate for ceramic green body production and is cheaper and safer compared to other polymers traditionally used for green body forming, such as polyethersulfone (PESf). Direct donor-doping of BaTiO_3 with 0.25 mol.% La and a 0.17 mol.% excess of TiO_2 , and without a calcination step, resulted in both a low room temperature resistivity and a sharp increase in the resistivity of approximately 3 orders of magnitude at the Curie temperature of BaTiO_3 . Self-heating experiments under an applied voltage showed that a PTCR hollow fiber bundle exhibited self-regulating power consumption characteristics. Hydrothermal synthesis of a zeolite X layer within the hollow fiber lumen was achieved. Adsorption studies revealed the zeolite layer to be predominantly ultramicroporous,

displaying strong interactions with CO_2 at 0°C .

Declaration of Competing Interest

The authors report no declarations of interest.

Acknowledgements

The authors gratefully acknowledge financial support from Horizon 2020 Marie Skłodowska-Curie Actions for funding of the Individual Fellowship SmartSorp project (Smart Ceramic Hollow Fibers for Energy Efficient Gas and Vapour Sorption), grant agreement no. 843988.

Appendix A. Supplementary data

Supplementary data associated with this article can be found, in the online version, at <https://doi.org/10.1016/j.jeurceramsoc.2021.10.049>.

References

- [1] S. Sircar, Applications of gas separation by adsorption for the future, *Adsorpt. Sci. Technol.* 19 (5) (2001) 347–366.
- [2] C.R. Reid, K.M. Thomas, Adsorption kinetics and size exclusion properties of probe molecules for the selective porosity in a carbon molecular sieve used for air separation, *J. Phys. Chem. B* 105 (43) (2001) 10619–10629.
- [3] J.G. Bell, M.J. Benham, K.M. Thomas, Adsorption of Carbon Dioxide, water vapor, nitrogen, and sulfur dioxide on activated carbon for capture from flue gases: competitive adsorption and selectivity aspects, *Energy Fuels* 35 (9) (2021) 8102–8116.
- [4] R.P. Lively, R.R. Chance, B.T. Kelley, H.W. Deckman, J.H. Drese, C.W. Jones, W. J. Koros, Hollow Fiber adsorbents for CO_2 removal from flue gas, *Ind. Eng. Chem. Res.* 48 (15) (2009) 7314–7324.
- [5] A.S. Bhowan, B.C. Freeman, Analysis and status of post-combustion carbon dioxide capture technologies, *Environ. Sci. Technol.* 45 (20) (2011) 8624–8632.
- [6] J.G. Bell, K. Angus, C. Todd, K.M. Thomas, Functional hollow Fiber adsorbent materials with a self-regulating composite outer layer for gas purification with energy efficient electrothermal regeneration, *Ind. Eng. Chem. Res.* 52 (3) (2013) 1335–1351.
- [7] R.T. Yang, *Gas Separation by Adsorption Processes*, Butterworths, Boston, 1987.
- [8] S.J.A. DeWitt, A. Sinha, J. Kalyanaraman, F.Y. Zhang, M.J. Realff, R.P. Lively, Critical comparison of structured contactors for adsorption-based gas separations, *Annu. Rev. Chem. Biomol. Eng.* 9 (2018) 129–152.
- [9] X.S. Feng, C.Y. Pan, C.W. McMinis, J. Ivory, D. Ghosh, Hollow-fiber-based adsorbents for gas separation by pressure-swing adsorption, *AIChE J.* 44 (7) (1998) 1555–1562.
- [10] M. Petkovska, M. Mitrovic, Microscopic modeling of electrothermal desorption, *Chem. Eng. J. Biochem. Eng. J.* 53 (3) (1994) 157–165.
- [11] K.D. Dombrowski, C.M.B. Lehmann, P.D. Sullivan, D. Ramirez, M.J. Rood, K. J. Hay, Organic vapor recovery and energy efficiency during electric regeneration of an activated carbon Fiber cloth adsorber, *J. Environ. Eng.* 130 (3) (2004) 268–275.
- [12] E. Andrich, Ptc thermistors as self-regulating heating elements, *Philips. Tech. Rev.* 30 (6–7) (1969) 170.
- [13] Y.L. Chen, S.F. Yang, PTCR effect in donor doped barium titanate: review of compositions, microstructures, processing and properties, *Adv. Appl. Ceram* 110 (5) (2011) 257–269.
- [14] J. Nowotny, M. Rekas, Positive temperature-coefficient of resistivity for Batio3-Based materials, *Ceram. Int.* 17 (4) (1991) 227–241.
- [15] B. Huybrechts, K. Ishizaki, M. Takata, The positive temperature-coefficient of resistivity in Barium-Titanate, *J. Mater. Sci.* 30 (10) (1995) 2463–2474.
- [16] W. Heywang, Barium titanate as a semiconductor with blocking layers, *Solid. Electron.* 3 (1) (1961) 51–58.
- [17] P.W. Haaymann, R.W. Dam, H.A. Klasens, in: --. German Patent 929, --. Netherlands Patent 84 (Eds.) 1955.
- [18] D.C. Sinclair, A.R. West, Impedance and Modulus spectroscopy of semiconducting Batio3 showing positive temperature-coefficient of resistance, *J. Appl. Phys.* 66 (8) (1989) 3850–3856.
- [19] G.H. Jonker, Some aspects of semiconducting barium titanate, *Solid. Electron.* 7 (12) (1964) 895–903.
- [20] X. Tan, Y. Liu, K. Li, Preparation of LSCF ceramic hollow-fiber membranes for oxygen production by a Phase-Inversion/Sintering technique, *Ind. Eng. Chem. Res.* 44 (1) (2005) 61–66.
- [21] N. Peng, N. Widjojo, P. Sukitpaneevit, M.M. Teoh, G.G. Lipscomb, T.-S. Chung, J.-Y. Lai, Evolution of polymeric hollow fibers as sustainable technologies: past, present, and future, *Prog. Polym. Sci.* 37 (10) (2012) 1401–1424.
- [22] K. Li, X. Tan, Y. Liu, Single-step fabrication of ceramic hollow fibers for oxygen permeation, *J. MembraneSci.* 272 (1) (2006) 1–5.

- [23] S.M. Liu, K. Li, R. Hughes, Preparation of porous aluminium oxide (Al₂O₃) hollow fibre membranes by a combined phase-inversion and sintering method, *Ceram. Int.* 29 (8) (2003) 875–881.
- [24] G.R. Guillen, Y.J. Pan, M.H. Li, E.M.V. Hoek, Preparation and characterization of membranes formed by nonsolvent induced phase separation: a review, *Ind. Eng. Chem. Res.* 50 (7) (2011) 3798–3817.
- [25] B. Wang, Z.P. Lai, Finger-like voids induced by viscous fingering during phase inversion of alumina/PES/NMP suspensions, *J. Membrane Sci.* 405 (2012) 275–283.
- [26] S. Mintova, N. Barrier, Verified Synthesis of Zeolitic Materials, Synthesis Commission of the International Zeolite Association, 2016.
- [27] R. Wasche, W. Denner, H. Schulz, Influence of high hydrostatic-pressure on the crystal-structure of barium-titanate (Batio₃), *Mater. Res. Bull.* 16 (5) (1981) 497–500.
- [28] F.D. Morrison, D.C. Sinclair, A.R. West, Electrical and structural characteristics of lanthanum-doped barium titanate ceramics, *J. Appl. Phys.* 86 (11) (1999) 6355–6366.
- [29] A.K. Holda, I.F.J. Vankelecom, Understanding and guiding the phase inversion process for synthesis of solvent resistant nanofiltration membranes, *J. Appl. Polym. Sci.* 132 (27) (2015).
- [30] M.A. Frommer, R.M. Messalem, Mechanism of membrane formation .6. Convective flows and large void formation during membrane precipitation, *Ind. Eng. Chem. Prod. Rd.* 12 (4) (1973) 328–333.
- [31] C.V. Sternling, L.E. Scriven, Interfacial turbulence - hydrodynamic instability and the marangoni effect, *AIChE J.* 5 (4) (1959) 514–523.
- [32] G.R. Guillen, G.Z. Ramon, H.P. Kayehpour, R.B. Kaner, E.M.V. Hoek, Direct microscopic observation of membrane formation by nonsolvent induced phase separation, *J. Membrane Sci.* 431 (2013) 212–220.
- [33] M.I. Mendelson, Average grain size in polycrystalline ceramics, *J. Am. Ceram. Soc.* 52 (8) (1969) 443–.
- [34] A.R.C. Gerlt, A.K. Criner, L. Semiatin, E.J. Payton, On the grain size proportionality constants calculated in MI Mendelson's "Average Grain Size in Polycrystalline Ceramics, *J. Am. Ceram. Soc.* 102 (1) (2019) 37–41.
- [35] B.C. LaCourse, V.R.W. Amarakoon, Characterization of the firing schedule for positive temperature coefficient of resistance BaTiO₃, *J. Am. Ceram. Soc.* 78 (12) (1995) 3352–3356.
- [36] D.L. Zhang, D.X. Zhou, S.L. Jiang, X. Wang, S.P. Gong, Effects of porosity on the electrical characteristics of current-limiting BaTiO₃-based positive-temperature-coefficient (PTC) ceramic thermistors coated with electrodeless nickel-phosphorous electrode, *Sens. Actuators a-Phys.* 112 (1) (2004) 94–100.
- [37] J.A. Varela, O.J. Whittemore, E. Longo, Pore size evolution during sintering of ceramic oxides, *Ceram. Int.* 16 (3) (1990) 177–189.
- [38] M. Perez-Page, J. Makel, K. Guan, S.L. Zhang, J. Tringe, R.H.R. Castro, P. Stroeve, Gas adsorption properties of ZSM-5 zeolites heated to extreme temperatures, *Ceram. Int.* 42 (14) (2016) 15423–15431.
- [39] X.C. Xu, W.S. Yang, J. Liu, L.W. Lin, N. Stroth, H. Brunner, Synthesis of NaA zeolite membrane on a ceramic hollow fiber, *J. Membrane Sci.* 229 (1–2) (2004) 81–85.
- [40] H. Yan, N.K. Ma, Z.Y. Zhan, Z.B. Wang, Fabrication of zeolite NaA membranes on hollow fibers using nano-sized seeds exfoliated from mesoporous zeolite crystals, *Microporous Mesoporous Mater.* 215 (2015) 244–248.
- [41] M. Thommes, K. Kaneko, A.V. Neimark, J.P. Olivier, F. Rodriguez-Reinoso, J. Rouquerol, K.S.W. Sing, Physisorption of gases, with special reference to the evaluation of surface area and pore size distribution (IUPAC Technical Report), *Pure Appl. Chem.* 87 (9–10) (2015) 1051–1069.
- [42] F. Rodriguez-Reinoso, A. Linares-Salano, *Microporous Structure of Activated Carbons As Revealed by Adsorption Methods*, Marcel Dekker, New York, 1989.
- [43] H. Marsh, Adsorption methods to study microporosity in coals and carbons - a critique, *Carbon* 25 (1) (1987) 49–58.
- [44] S.G. Chen, R.T. Yang, Theoretical basis for the potential-theory adsorption-isotherms - the dubinin-radushkevich and dubinin-astakhov equations, *Langmuir* 10 (11) (1994) 4244–4249.
- [45] J.H. Cole, D.H. Everett, C.T. Marshall, A.R. Paniego, J.C. Powl, F. Rodriguez-Reinoso, Thermodynamics of the high temperature adsorption of some permanent gases by porous carbons, *J. Chem. Soc. Faraday Trans. 1* 70 (0) (1974) 2154–2169.
- [46] L. Czepirski, J. Jagiello, Virial-type thermal equation of gas solid adsorption, *Chem. Eng. Sci.* 44 (4) (1989) 797–801.
- [47] A.M. Williams, J. Walker, The adsorption of gases at low and moderate concentrations. Part I.—Deduction of the theoretical adsorption isostere and isotherm. Part II.—Experimental verification of the form of the theoretical isosteres and isotherms, *Proc. R. Soc., Lond., Ser. A* 96 (677) (1919) 287–297.
- [48] D.C. Henry, LX. A kinetic theory of adsorption, *London, Edinburgh Dublin Philos. Mag. J. Sci.* 44 (262) (1922) 689–705.
- [49] C.R. Reid, K.M. Thomas, Adsorption of gases on a carbon molecular sieve used for air separation: linear adsorptives as probes for kinetic selectivity, *Langmuir* 15 (9) (1999) 3206–3218.
- [50] C.E. Webster, R.S. Drago, M.C. Zerner, Molecular dimensions for adsorptives, *J. Am. Chem. Soc.* 120 (22) (1998) 5509–5516.
- [51] H. Kim, H.S. Cho, C. Kim, M. Choi, Gradual disordering of LTA zeolite for continuous tuning of the molecular sieving effect, *J. Phys. Chem. C* 121 (12) (2017) 6807–6812.
- [52] F.D. Morrison, D.C. Sinclair, A.R. West, Characterization of lanthanum-doped barium titanate ceramics using impedance spectroscopy, *J. Am. Ceram. Soc.* 84 (3) (2001) 531–538.
- [53] M. Iijima, N. Sato, M. Tsukada, H. Kamiya, Dispersion behavior of barium titanate nanoparticles prepared by using various polycarboxylic dispersants, *J. Am. Ceram. Soc.* 90 (9) (2007) 2741–2746.
- [54] M. Kuwabara, Determination of the potential barrier height in barium-titanate ceramics, *Solid. Electron.* 27 (11) (1984) 929.
- [55] Z.S. Larasati, N. Widiastuti, Adsorption-desorption of CO₂ and H₂ gases on ZeoliteX supported on glass fiber, in: *The 3rd International Seminar on Chemistry, AIP Conference Proceedings* 2049, 020083, 2018.